Braz J Phys (2014) 44:73–90
DOI 10.1007/s13538-013-0162-x

NUCLEAR PHYSICS

Analysis of ^{6}Li Scattering at 600 MeV

M. El-Azab Farid · K. O. Behairy · Z. M. M. Mahmoud · Kasem Omar Hussein

Received: 15 April 2013 / Published online: 18 December 2013

Abstract The elastic and inelastic scattering of ^{6}Li on ^{12}C, ^{58}Ni, ^{90}Zr, and ^{208}Pb targets at 600 MeV are analyzed via double-folding optical model potentials based on the S1Y effective nucleon–nucleon (NN) interaction and $t\rho\rho$ approximation. Information is provided, by single- and coupled-channel calculations, on the effect of breakup and its feedback on the elastic scattering of ^{6}Li ions. Experimental results are successfully reproduced. The in-medium NN cross-section and second-order (double-scattering) correction to the $t\rho\rho$ potential are taken into account. Reaction cross-sections are computed from exact and approximate solutions.

Keywords ^{6}Li elastic and inelastic scattering · Optical model · Folding model

1 Introduction

During the last three decades, the elastic scattering and inclusive breakup of light ions on heavy target nuclei have been extensively studied both theoretically and experimentally [1–3]. Nuclear reactions of energetic projectiles with low breakup thresholds are currently investigated with new vigor in view of possible access to fusion reactions of astrophysical interest at stellar energies [4]. Since breakup is expected to be the dominant direct-reaction process for weakly bound projectiles, its effect on other reaction channels, especially on the fusion process, has recently been intensively investigated [3]. Due to the particular nuclear structure of the ^{6}Li nucleus, ^{6}Li-induced reactions provide a unique opportunity to study specific features of the nuclear reaction mechanism, in particular the role of breakup processes and their feedback on other reaction channels [5–7]. The investigation of ^{6}Li elastic scattering is of considerable interest, not only because of the striking failure of the DF model to predict their data as pointed by Satchler and Love [8], which was attributed to the effect of the breakup of the loosely bound ^{6}Li nucleus, but also because the ^{6}Li ion occupies an intermediate position in the mass number range A=4–12 of ions whose elastic scattering exhibit a transition between the ranges characteristic of light ions ($A \leq 4$) and of heavy ions (HI) ($A \geq 12$) [9]. Coupled discretized continuum channel (CDCC) studies [5] have shown that the breakup effect is the key to understanding the experimental cross-sections in the low-energy region, where the elastic and breakup channels are strongly coupled, the coupling being expected to decrease with increasing incident energy. In a CDCC study at E_{lab}=100A MeV using the cluster folding model [10], the breakup channels were predicted to decouple from the elastic-reaction channel at intermediate energies [11]. A theoretical investigation of the projectile-breakup effect on ^{6}Li elastic scattering using CDCC calculations with a potential constructed from the DDM3Y interaction [12] in a double-folding model (DFM) showed that the breakup effect becomes less important, albeit not completely negligible, even at E_{lab}= 100A MeV [16]. The diminishing significance of the breakup effect with increasing energy can be traced to the decrease of the coupling potentials for breakup channels [2].

Recent valuable experimental data for elastic scattering and inclusive breakup of ^{6}Li particles on ^{12}C, ^{58}Ni, ^{90}Zr, and ^{208}Pb

M. E.-A. Farid
Physics Department, Assiut University, Assiut 71516, Egypt

K. O. Behairy
Physics Department, Aswan University, Aswan Branch, Aswan, Egypt

Z. M. M. Mahmoud
Physics department, Fculty of science, Asiut University, New Valley, Al-Kharga, Egypt

K. O. Hussein (✉)
Aswan University, Aswan, Egypt
e-mail: drkasemomar@yahoo.com

targets at 100A MeV have been studied by Schwarz et al. [2]. The fragmentation of ^{6}Li into an α-particle and a deuteron was observed as a prominent reaction channel at this energy. The CDCC calculations, analogous to single-channel optical model calculations, were carried out with DFM potentials based upon the DDM3Y [17, 18] effective interaction. Coupling to breakup reactions was found at projectile energies above 100A MeV, although it was reduced in comparison with the lower-energy effect. The authors also investigated the effects of target excitation in the case of ^{12}C targets and showed that these effects are completely negligible in comparison with ^{6}Li breakup. For other targets, all of which are closed-shell nuclei, the excitation effects are expected to be even smaller.

In three successive studies [13–15], DF potentials based upon four different NN interactions, M3Y [17], S1Y [19], KH [20], and JLM [21], were generated. Twenty-six sets of data for the angular distribution of ^{6,7}Li elastic scattering differential cross-section at intermediate energies were analyzed, and successful predictions for the observed cross-sections were obtained. For the sake of comparison, besides the distorted-wave Born approximation (DWBA), an analysis of the coupled channels (CC) mechanism was also carried out to investigate the effect of coupling to the inelastic channels upon elastic-scattering calculations. Eight sets of ^{6,7}Li inelastic scattering data in the energy range 12–35 MeV/nucleon from different targets were analyzed using DF optical potentials based on the S1Y interaction [15].

Here, we extend previous studies [13–15] to test the performance of the DF optical model potentials in analyses of the ^{6}Li elastic- and inelastic-scattering processes at intermediate energies. We analyze four scattering systems: elastic and inelastic scattering of ^{6}Li on ^{12}C, ^{58}Ni, ^{90}Zr, and ^{208}Pb targets at 600 MeV. At high and intermediate bombarding energies, the nuclear densities can be directly related to the optical potential, as long as the effects of multiple NN scattering can be neglected. The effective interaction is taken to be the free NN t-matrix scattering amplitude, which is referred to as the impulse approximation [22, 23] or $t\rho\rho$ approximation [24].

Beside the phenomenological potentials, we have generated microscopic DF potentials on the basis of the S1Y [19] effective interaction and $t\rho\rho$ approximation [24, 25]. We have considered the in-medium *NN* cross-section and second-order (double-scattering) corrections to the $t\rho\rho$ potentials. We have computed differential and total reaction cross-sections from the exact and approximate solutions. To investigate the effect of coupling to inelastic scattering on elastic scattering, we have studied the low excited state 2^{+} for the ^{6}Li+^{12}C reaction at 100A MeV. We have also determined the target mass-number dependence of the real and imaginary volume integrals, as well as the total reaction cross-section.

The manuscript is organized as follows: In the next section, the theoretical formalism is presented, while our procedure is explained in Section 3. Results and discussion are presented in Section 4, and general conclusions are summarized in Section 5.

2 Formalism

2.1 The Model

The Schrödinger equation, which describes the nucleus–nucleus scattering through a total effective potential $U(R)$ takes the form

$$\left[-\frac{h^2}{2\mu}\nabla^2 + U(R) - E_{\mathrm{CM}}\right]\Psi(R) = 0. \tag{1}$$

The asymptotic behavior of its solutions $\psi(R)$ describes the projectile–target elastic scattering; μ is the reduced mass of the system when the projectile and target are well separated, and E_{CM} is the energy of the relative motion in the center-of-mass (c.m) frame. From the solution of this equation, we get the scattering amplitude $f(\theta)$, which can be written as a sum of Coulomb and nuclear scattering amplitudes,

$$f(\theta) = f_{\mathrm{C}}(\theta) + f_{\mathrm{N}}(\theta) = f_{\mathrm{C}}(\theta) + \frac{1}{2ik}\sum (2L+1)\left(e^{2i\sigma_{\mathrm{L}}}\right)(S_L - 1)P_L(\cos\theta), \tag{2}$$

where the total reaction cross-section is defined as

$$\sigma_{\mathrm{R}} = \frac{\pi}{k^2}\sum_{L=0}^{\infty}(2L+1)\left(1 - |S_L|^2\right) \tag{3}$$

where $S_L = \exp(-2i\delta_L)$ is the scattering matrix and δ_L is the nuclear phase shift. In the Glauber eikonal approximation

Table 1 Parameters for the nucleon–nucleon scattering amplitude

E (MeV/nucleon)	σ^{T}_{NN}(fm^2)	α_{NN}	a_{NN} (fm^2)
30	19.6	0.87	
38	14.6	0.89	
40	13.5	0.9	
49	10.4	0.94	
85	6.1	1.0	
94	5.5	1.07	0.51
120	4.5	0.7	0.58
200	3.2	0.6	0.062
342.5	2.84	0.26	0.31
425	3.2	0.36	0.24
550	3.62	0.04	0.062
650	4.0	−0.095	0.08
800	4.26	−0.075	0.105
1000	4.32	−0.275	0.105
2200	4.33	0.33	0.13

[26, 27], the semi-classical relation between the impact parameter b and the angular momentum L [28] yields the following expression for the total reaction cross-section

$$\sigma_{\mathrm{R}} = 2\pi \int_0^{\infty} \mathrm{bdb}\left\{1 - e^{-2\mathrm{i}\chi(b)}\right\}. \tag{4}$$

The optical potential $V(R)$ for nucleus–nucleus scattering in the DF model is defined by the expression

$$V^{DF}_{A_1A_2}(R) = \int \widetilde{n}_{A1}(r_1)\widetilde{n}_{A2}(r_2)\upsilon_{nn}(s,E)dr_1^r dr_2^v \tag{5}$$

where $\widetilde{n}_{A_1}(r_1)$ and $\widetilde{n}_{A_2}(r_2)$ are the matter density distributions of both the target and projectile nuclei, respectively, and $\upsilon_{nn}(s, E)$ is the effective NN interaction with $s = |R^v - r_1^v + r_2^v|$, and E_{Lab} is the laboratory bombarding nucleon energy.

2.2 The Nuclear Matter Density Distributions

The nuclear density of ^{6}Li nucleus is written in the form [29]

$$\rho^{^6Li}_{A_1}(r_1) = 0.203\exp\left(0.330r_1^2\right) + \left[0.0131 + 0.00137r_1^2\right]\exp\left(0.1584r_1^2\right), \tag{6}$$

which has been constructed from the proton charge distribution deduced from the phenomenological electron scattering with the assumption that ^{6}Li proton and neutron densities are equal at $N=Z$. The resulting root mean square (rms) radius is $\langle r^2\rangle^{1/2} = 2.394fm$.

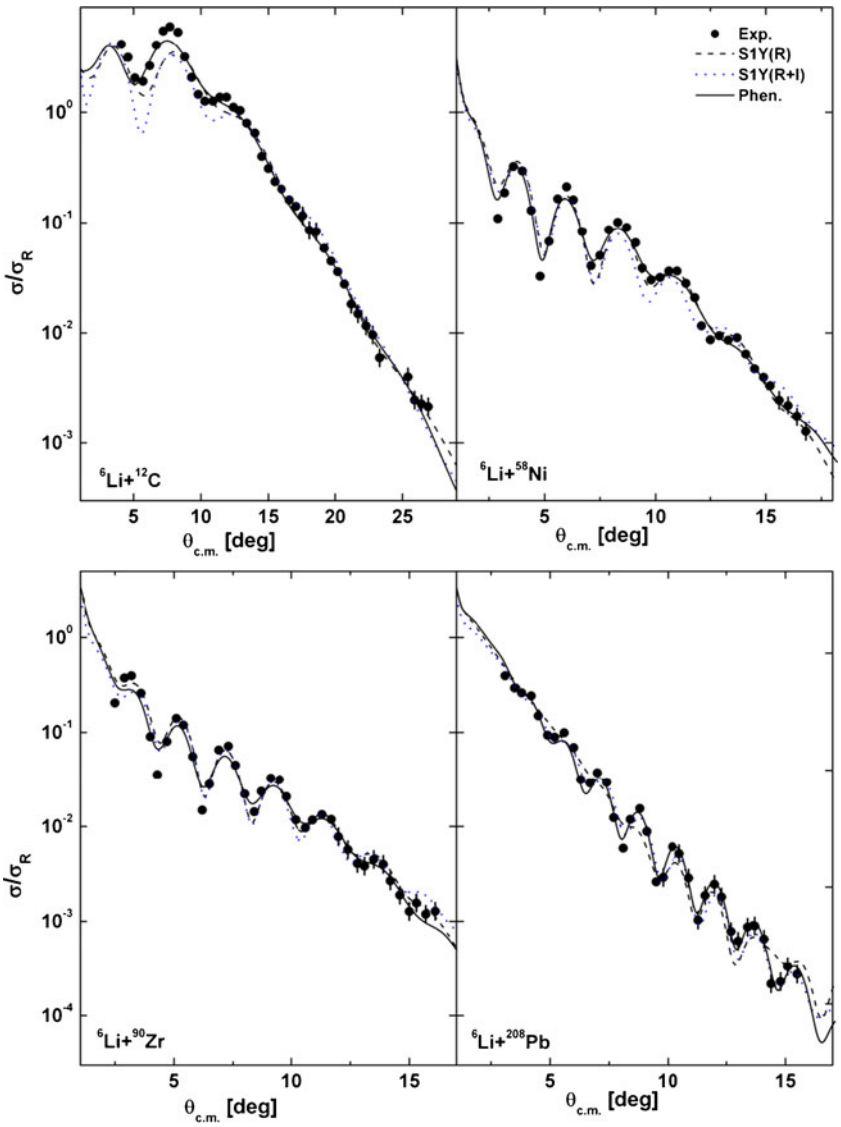

Fig. 1 Measured angular distributions of the elastic ^{6}Li scattering on ^{12}C, ^{58}Ni, ^{90}Zr, and ^{208}Pb targets compared with predictions of the DF optical potentials based upon real (*dashed lines*) and complex (*dotted lines*) S1Y effective NN interaction besides phenomenological potential results (*sold lines*). Data are from Schwarz [2]

For all the target densities, we use the two-parameter Fermi-model (FM) form, defined as

$$\rho_2(r_2) = \rho_0\left[1-\exp\left(\frac{r_2-c}{a}\right)\right]^{-1}$$

The parameters ρ_0, c, and a and the corresponding $\langle r^2\rangle^{1/2}$ for ^{12}C, ^{58}Ni [30], ^{90}Zr, and ^{208}Pb [12] nuclei are listed in El-Azab Farid and Hassanain [13], where $\rho_0=3/\{4\pi c^3[1+(\pi^2d^2/c^2)]\}$. Here, d is the diffuseness and c is the half-value radius in terms of the rms radius R for the FM distribution, calculated from the equality $c=[(5/3R)^2-(7/3)\pi^2d^2-(5/3)r_p^2]^{1/2}$, where r_P is the proton radius [31].

2.3 The Effective NN Interaction

2.3.1 The S1Y Effective NN Interaction

The S1Y effective NN interaction has the phenomenological form [19]

$$\upsilon_{\rm nn}(s) = (\upsilon + iw)\frac{\exp(-s/t)}{s/t}\text{MeV}, \quad (8)$$

where υ and w are the real and imaginary strengths, s (in fm) is the NN separation, and t (in fm) is the range of the interaction.

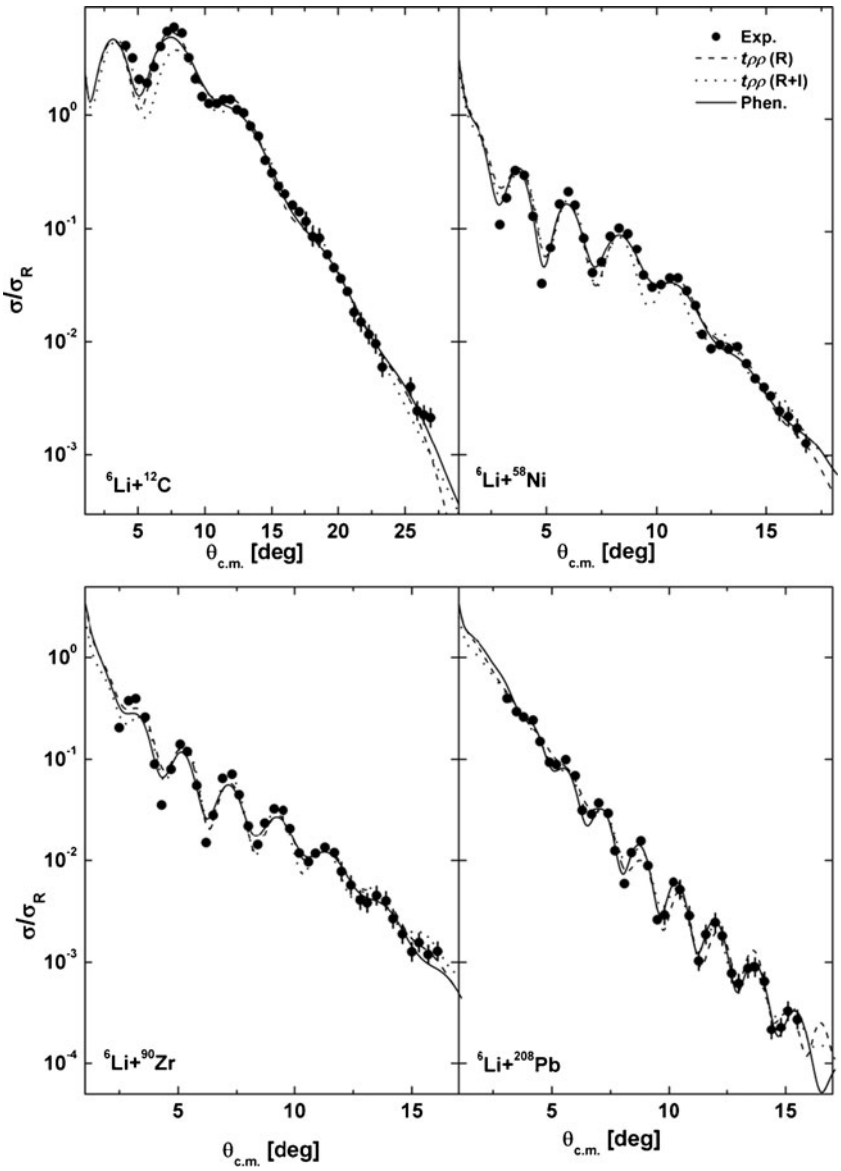

Fig. 2 Measured angular distributions, as in Fig. 1, but for the $t\rho\rho$ approximation

2.3.2 The tρρ Approximation

To obtain the nucleus–nucleus $t\rho\rho$ interaction, we insert the NN G or T-matrix in the DF calculation. Thus, we write

$$V^{(1)}_{A_1A_2}(R)\cong t\left(\theta=0^0;E\right)\int dr'\rho_{A_1}\left(r'\right)\rho_{A_2}\left(R-r'\right) = -4\pi\frac{E}{k^2}f_{NN}\left(\theta=0^0;E\right)\int dr'_1\rho_{A_1}\left(r'\right)\rho_{A_2}\left(R-r'\right) \quad (9)$$

where $f_{NN}(\theta)$ is the NN scattering amplitude. With the help of the optical theorem, one may obtain the imaginary part of $V^{(1)}_{A_1A_2}(R)$ as

$$\mathrm{Im}V^{(1)}_{A_1A_2}(R) = -\frac{E}{k}\sigma_{NN}(E)\int\rho_{A_1}\left(r'\right)\rho_{A_2}\left(R-r'\right)dr', \quad (10)$$

and the real part of $V^{(1)}_{A_1A_2}(R)$ can be obtained from the equality

$$\mathrm{Re}f_{\mathrm{NN}} = \alpha\mathrm{Im}f_{\mathrm{NN}}, \mathrm{Im}f_{\mathrm{NN}} = \left(k\sigma^T_{\mathrm{NN}}/4\pi\right)\exp\left(-a_{\mathrm{NN}}q^2\right) \quad (11)$$

The NN cross-sections σ_{NN}, α_{NN}, and a_{NN} used to construct the optical potential in the "$t\rho\rho$" approximation are

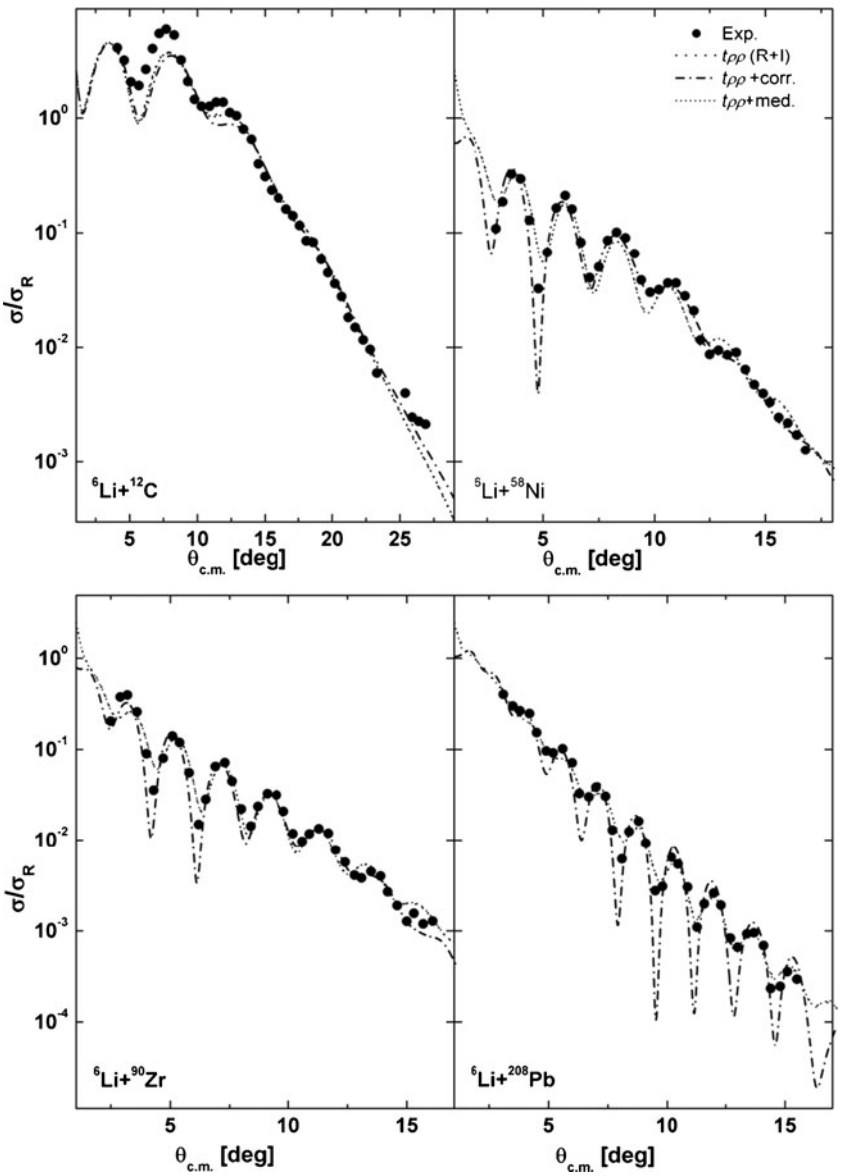

Fig. 3 Measured angular distributions, as in Fig. 2, but for complex $t\rho\rho$(R+I) approximated potentials (*dotted lines*), after adding the second-order potential correction (*dashed dotted lines*) and after introducing the in-medium effect correction (*short dashed lines*)

shown in Table 1. For energies lower than 94A MeV, $a_{NN}=0.5$ fm^2. The second-order (double-scattering) contribution to the ion–ion potential is given by the expression

$$V^{(2)}_{A_1A_2}(R) = -(iK/4E)R_{corr}\left(\int\left[V_{NA_1}\left(R-r'\right)\right]^2\rho_{A_2}\left(r'\right)dr' + \int\left[V_{NA_2}\left(R-r'\right)\right]^2\rho_{A_1}\left(r'\right)dr'\right) \quad (12)$$

where $V^{(1)}_{NA_1}(R)$ is the nucleon-nucleus (A_1) potential ($t\rho$). The imaginary and real parts of the second-order nucleus–nucleus potential are

$$\begin{aligned}
&\mathrm{Re}\,V^{(2)} = -(E/2k)\,|R_{\mathrm{corr}}|\,\alpha\,\sigma_T^2\left\langle\rho^2_{A_1}\rho_{A_2}+\rho^2_{A_2}\rho_{A_1}\right\rangle(R)\\
&\mathrm{Im}\,V^{(2)} = -(E/4k)|R_{\mathrm{corr}}|(\alpha-1)\,\sigma_T^2\left\langle\rho^2_{A_1}\rho_{A_2}+\rho^2_{A_2}\rho_{A_1}\right\rangle(R)\\
&\left\langle\rho^2_{A_1}\rho_{A_2}+\rho^2_{A_2}\rho_{A_1}\right\rangle(R) = \int\rho^2_{A_2}(R-r')\rho_{A_2}(r')dr'+\int\rho^2_{A_2}(R-r')\rho_{A_1}(r')dr'
\end{aligned} \quad (13)$$

where R_{corr} [24, 25] is composed of four distinct contributions,

$$R_{\mathrm{corr}} = R_{\mathrm{Pauli}} + R_{\mathrm{SRD}} + R_{\mathrm{PSR}} + R_{\mathrm{CM}}. \quad (14)$$

As explained by Boridy and Feshbach [32], R_{Pauli} is related to the Pauli exclusion-principle correlations, R_{SRD} is related to the short-range dynamical correlations, and R_{PSR} is connected to the combination of the

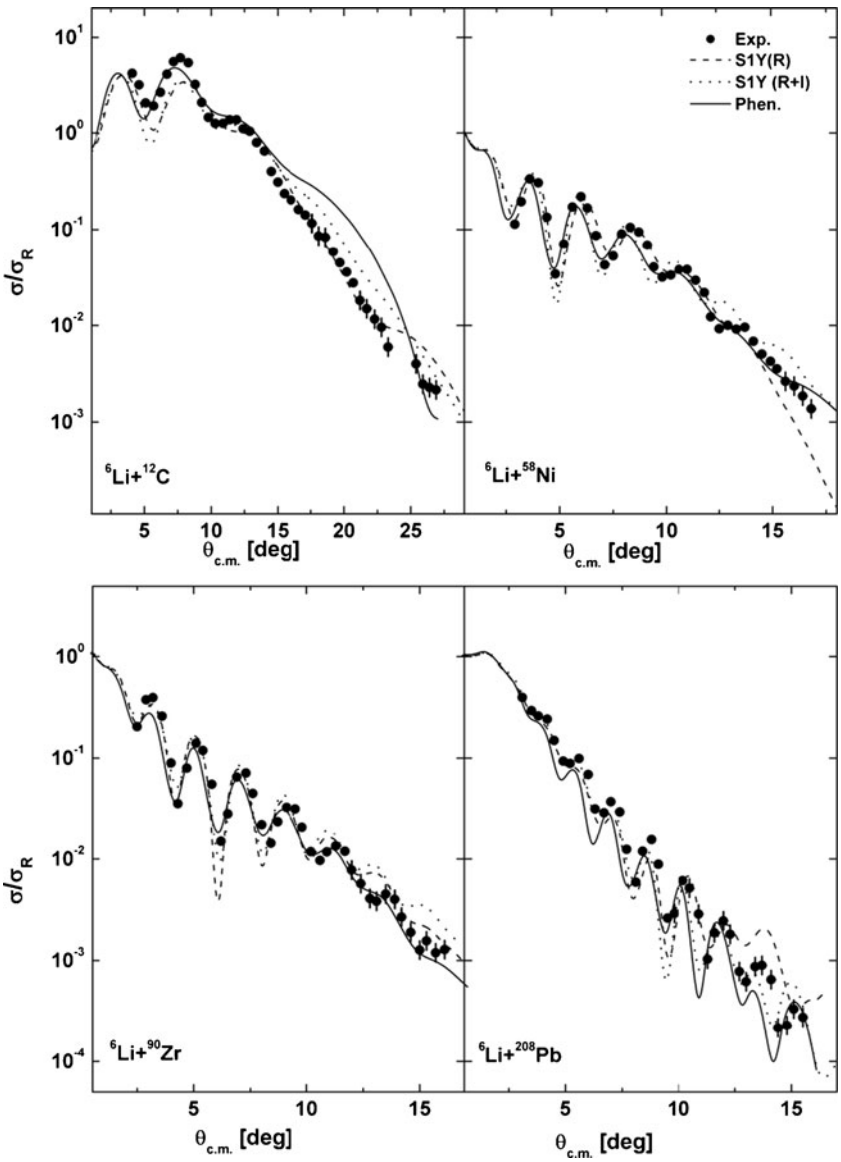

Fig. 4 Measured angular distributions, as in Fig. 1, but using the eikonal approximation

Pauli and a short-range dynamical term. Finally, R_{CM} arises from center of mass correlations. The approximate expressions for these four contributions to R_{corr} are derived [24, 25] in the form

$$-R_{Pauli} = \frac{1}{2}\left(1 - \frac{5}{A} + \frac{4}{A^2}\right)\frac{3\pi}{10k_F(r)}\frac{1}{1+\frac{8}{5}\overline{B}k_F^2(r)},$$

$$-R_{SRD} = \frac{1}{2}\left(1 - \frac{2}{A} + \frac{1}{A^2}\right)\sqrt{\pi}\frac{b^3}{b^2+8\overline{B}},$$

$$R_{PSR} = \frac{1}{2}\left(1 - \frac{5}{A} + \frac{4}{A^2}\right)\frac{3\pi}{10}\left(k_F^2(r) + \frac{5}{b^2}\right)^{-\frac{1}{2}}\left[1 + 8\overline{B}\left(\frac{k_F^2(r)}{5} + \frac{1}{b^2}\right)\right]^{-1},$$

$$-R_{CM} = \left(1 - 2/A + 1/A^2\right)_c,$$

where the parameters $A, k_F(r)\overline{B}, b, l_c$ are the target mass number, local Fermi momentum, finite-range parameter of NN elastic t-matrix, short-range dynamical correlation parameter and the effective "correlation length," respectively.

2.3.3 The Medium Effect

A new phenomenological formula to calculate the in-medium NN cross-section over a wide energy range based on several recent theoretical studies is proposed as [33]:

$$\gamma = \frac{E_{lab}}{931.5} + 1.0, \quad \beta = \sqrt{1.0 + \frac{1.0}{\gamma^2}} \tag{16}$$

where σ_{nn} is the neutron–neutron (or proton–proton) cross-section, σ_{np} is neutron–proton cross-section, ρ is nuclear matter density in cubic fm units, E_{lab} is the incident energy

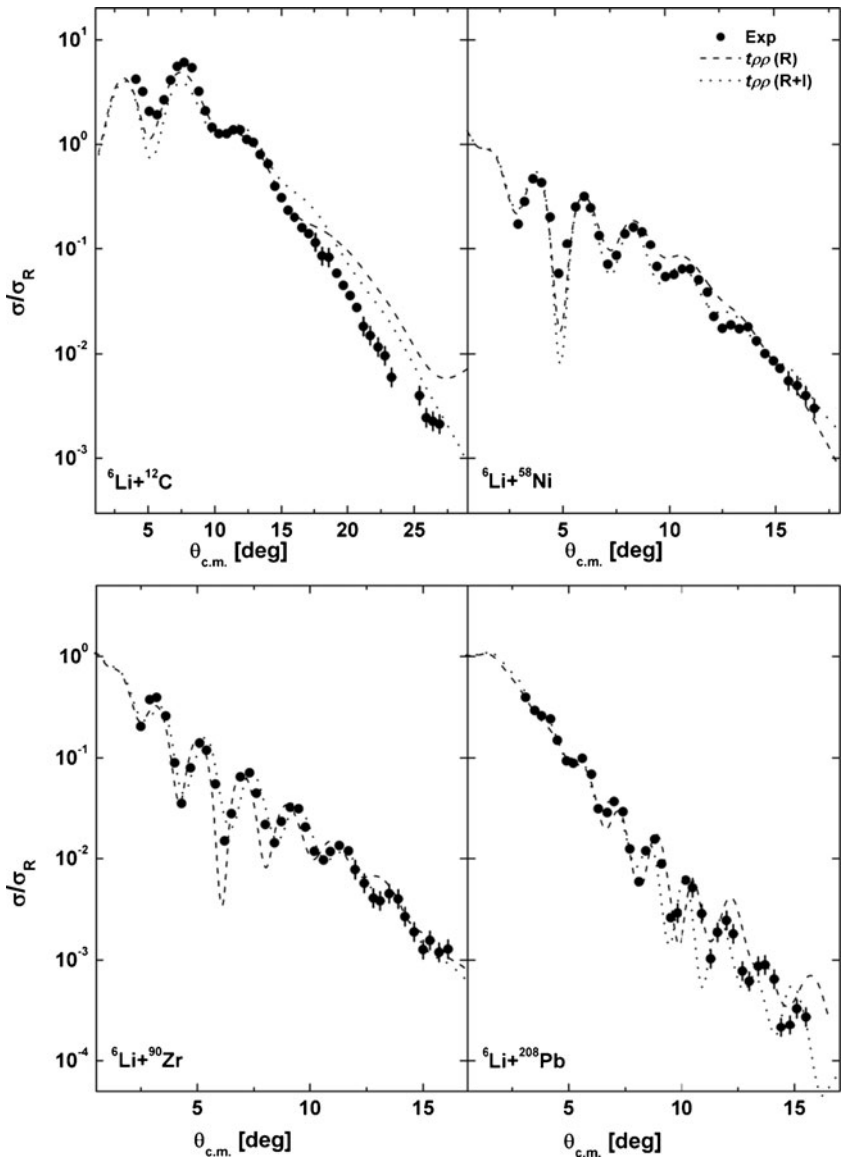

Fig. 5 Measured angular distributions, as in Fig. 2, but using the eikonal approximation

in the lab frame, and β is the ratio of the projectile velocity to the speed of light.

2.4 Deformed Optical Potential Model

Inelastic scattering measurements are usually analyzed using a deformed optical-model potential (DP) [22, 34]. This provides a transition potential whose radial dependence is

$$U_1^{\mathrm{DP}}(r) = -\delta_1^U \frac{dU(r)}{dr}$$

$$\sigma_{\mathrm{nn}}(E,\rho) = \left[\left(13.73 - 15.04\beta^{-1} + 8.76\beta^{-2} + 68.6\beta^{4}\right)\left[\frac{1.0 + 7.772E_{\mathrm{lab}}^{0.06}\rho^{1.48}}{1.0 + 18.01\rho^{1.46}}\right]\right]$$

$$\sigma_{\mathrm{np}}(E,\rho) = \left[\left(-70.67 - 18.18\beta^{-1} + 25.26\beta^{-2} + 113.85\beta\right)\left[\frac{1.0 + 20.88E_{\mathrm{lab}}^{0.04}\rho^{2.02}}{1.0 + 35.86\rho^{1.90}}\right]\right] \quad (17)$$

where the deformation length δ_1^U determines the strength of the interaction and $U(r)$ is the complex optical potential determined by the measured elastic scattering. The shape of $U_1^{\mathrm{DP}}(r)$ is independent of the multipolarity 1. The transition density $\rho_1^{\mathrm{tr}}(r)$ is given by the equation

$$\rho_1^{\mathrm{tr}}(r) = \delta_1^m \frac{d\rho(r)}{dr} \quad (18)$$

where $\rho(r)$ is the ground state density and δ_1^m is its 2^1-pole deformation length.

3 Procedure

To analyze the ^{6}Li elastic scattering data, we have first derived the real and imaginary phenomenological

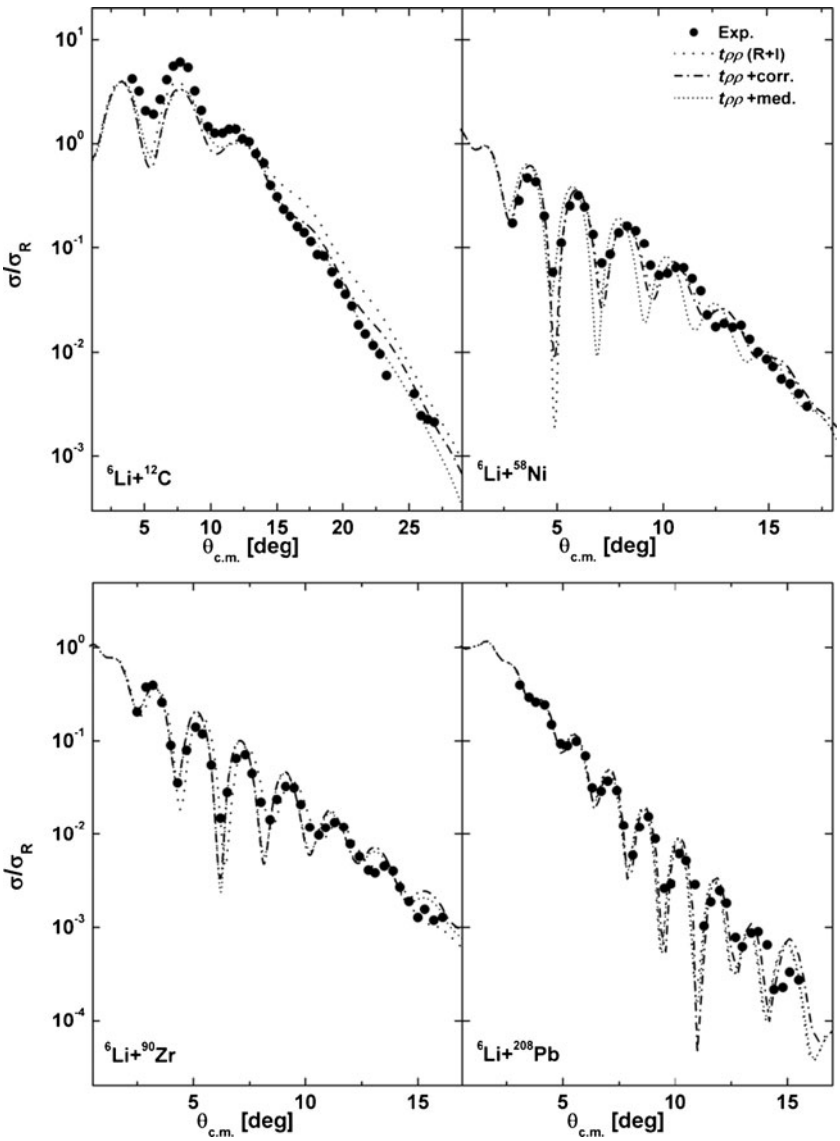

Fig. 6 Measured angular distributions, as in Fig. 3, but using the eikonal approximation

Table 2 Best-fit optical potential parameters extracted from the analysis of elastic ^{6}Li ion scattering using an exact solution

χ^2	σ_R (mb)	$-J_I$ (MeV fm^3)	a_W (fm)	r_W (fm)	$W_0(w)$ (MeV)	N_I	$-J_R$ (MeV fm^3)	a_V (fm)	r_V (fm)	$V_0(v)$ (MeV)	N_R	Potential
^{6}Li±^{12}C												
4.5	724	128	0.757	0.761	45.7		180.0			42.6		S1Y(R)
8.5	774	168.5			40.0		177.3			42.0		S1Y(R+I)
4.1	891	131.5	0.779	1.037	22.0		222.4				0.73	$t\rho\rho$(R)
5.9	723	143.0				0.60	174.4				0.57	$t\rho\rho$(R+I)
6.6	687	123.6				0.55	158.5				0.40	$t\rho\rho$(corr.)
6.0	718	142.9				0.40	171.5				0.40	$t\rho\rho$(med)
2.6	891	126.6	0.847	0.99	22.6		235.1	0.945	0.581	115.3		Phen.
^{6}Li±^{58}Ni												
5.8	1,987	113.2	0.944	1.019	38.3		203.7			48.4		S1Y(R)
8.1	1,795	215.2			51.1		202.6			48.1		S1Y(R+I)
5.5	2,047	108.3	0.988	1.037	34.3		196.6				0.65	$t\rho\rho$(R)
7.6	1,755	211.1				0.90	199.1				0.65	$t\rho\rho$(R+I)
11.0	1,769	226.8				1.04	183.2				0.43	$t\rho\rho$(corr.)
8.0	1,754	215.6				0.60	199.4				0.46	$t\rho\rho$(med)
2.0	1,935	108.2	0.92	1.017	37.1		218.2	1.099	0.672	178.2		Phen.

potentials in a six-parameter Woods-Saxon (WS) volume form as

$$U(R) = V_0/[1+\exp(R-R_v/a_v)] + W_0/[1+\exp(R-R_I/a_I)],$$
$$R_{v(I)} = r_{v(I)}\left(A_P^{1/3} + A_T^{1/3}\right) \quad (19)$$

where V_0, W_0, $r_{v(I)}$ and $a_{v(I)}$, A_P, and A_T are the real and imaginary depths in mega-electron volts, real and imaginary radii parameters in fm, real and imaginary diffuseness parameters in fm, the projectile, and the target mass numbers, respectively. We performed the automatic search using the computer code HI-OPTIM-94 [35] in order to minimize chi squared, defined as

$$\chi^2 = \frac{1}{N}\sum_{i=1}^{N}\left[\frac{\sigma(\theta_i)^{\text{cal}} - \sigma(\theta_i)^{\text{exp}}}{\Delta\sigma(\theta_i)}\right]^2, \quad (20)$$

where N is the number of differential cross-section data points, and $\sigma(\theta_i)^{\text{cal}}$ is the calculated cross-section. In Eq. 20, $\sigma(\theta_i)^{\text{exp}}$ and $\Delta\sigma(\theta_i)$ are the corresponding experimental

Table 3 Best-fit optical potential parameters, as in Table 2, but for ^{90}Zr and ^{208}Pb targets

χ^2	σ_R (mb)	$-J_I$ (MeV fm^3)	a_W (fm)	r_W (fm)	$W_0(w)$ (MeV)	N_I	$-J_R$ (MeV fm^3)	a_V (fm)	r_V (fm)	$V_0(v)$ (MeV)	N_R	Potential
^{6}Li±^{12}C												
4.5	724	128	0.757	0.761	45.7		180.0			42.6		S1Y(R)
8.5	774	168.5			40.0		177.3			42.0		S1Y(R+I)
4.1	891	131.5	0.779	1.037	22.0		222.4				0.73	$t\rho\rho$(R)
5.9	723	143.0				0.60	174.4				0.57	$t\rho\rho$(R+I)
6.6	687	123.6				0.55	158.5				0.40	$t\rho\rho$(corr.)
6.0	718	142.9				0.40	171.5				0.40	$t\rho\rho$(med)
2.6	891	126.6	0.847	0.99	22.6		235.1	0.945	0.581	115.3		Phen.
^{6}Li±^{58}Ni												
5.8	1,987	113.2	0.944	1.019	38.3		203.7			48.4		S1Y(R)
8.1	1,795	215.2			51.1		202.6			48.1		S1Y(R+I)
5.5	2,047	108.3	0.988	1.037	34.3		196.6				0.65	$t\rho\rho$(R)
7.6	1,755	211.1				0.90	199.1				0.65	$t\rho\rho$(R+I)
11.0	1,769	226.8				1.04	183.2				0.43	$t\rho\rho$(corr.)
8.0	1,754	215.6				0.60	199.4				0.46	$t\rho\rho$(med)
2.0	1,935	108.2	0.92	1.017	37.1		218.2	1.099	0.672	178.2		Phen.

Table 4 Optical potential parameters obtained from the eikonal-approximation calculations

σ_R (mb)	a_W (fm)	r_W (fm)	$W_0(w)$ (MeV)	N_I	a_V (fm)	r_V (fm)	$V_0(v)$ (MeV)	N_R	Potential
^{6}Li±^{12}C									
705	0.847	0.99	22.7				42.6		S1Y(R)
783			39.9				42.0		S1Y(R+I)
859	0.779	1.037	27.2					0.73	$t\rho\rho$(R)
810				0.82				0.63	$t\rho\rho$(R+I)
795				0.82				0.42	$t\rho\rho$(corr)
747				0.44				0.37	$t\rho\rho$(med)
946	0.847	0.99	22.7		0.945	0.581	115.3		Phen.
^{6}Li±^{58}Ni									
1,751	0.92	1.017	44.5				48.4		S1Y(R)
1,810			51.1				48.1		S1Y(R+I)
1,853	0.92	1.017	48.3					0.65	$t\rho\rho$(R)
1,702				0.75				0.58	$t\rho\rho$(R+I)
1,723				0.9				0.4	$t\rho\rho$(corr)
1,846				0.75				0.45	$t\rho\rho$(med)
1,950	0.92	1.017	37.1		1.099	0.672	178.2		Phen.
^{6}Li±^{90}Zr									
2,401	0.878	1.012	58.2				50.3		S1Y(R)
2,189			51.2				50.6		S1Y(R+I)
2,520	0.878	1.012	57.3					0.66	$t\rho\rho$(R)
1,930				0.54				0.5	$t\rho\rho$(R+I)
2,046				0.8				0.4	$t\rho\rho$(corr)
2,077				0.53				0.42	$t\rho\rho$(med)
2,310	0.878	1.012	47.7		1.09	0.715	207.2		Phen.
^{6}Li±^{208}Pb									
3,759	0.733	1.096	46.7				44.1		S1Y(R)
3,184			44.2				45.0		S1Y(R+I)
4,107	0.733	1.096	46.7					0.52	$t\rho\rho$(R)
3,141				0.8				0.6	$t\rho\rho$(R+I)
3,103				0.8				0.4	$t\rho\rho$(corr)
3,120				0.53				0.42	$t\rho\rho$(med)
3,219	0.733	1.096	46.7		1.055	0.826	223.5		Phen.

cross-section and its relative uncertainty, respectively. The χ^2 values were obtained considering uniform 10 % error for all analyzed data.

In the second step, we used the DF optical potentials generated from Eq. 5. The following procedures were considered:

1. We neglected the spin-orbit potential, to which the elastic scattering cross-section data are insensitive in this energy range [36].
2. All the S1Y calculations used a fixed range at t=0.7 fm, and the depths v and w have been optimized in order to fit

Table 5 Quadrupole deformation length extracted from the analysis of ^{6}Li inelastic scattering to the first (2+, 4.44 MeV) excited state of ^{12}C at 600 MeV using the DWBA treatment

δ_2^W (fm)	β_2	a_W (fm)	r_W (fm)	W_0 (MeV)	N_I	a_V (fm)	r_V (fm)	V_0 (MeV)	N_R	Potential
0.9	0.38	0.997	0.99	17.65				48.		S1Y(R)
0.8	0.36	0.997	0.99	17.65					0.71	$t\rho\rho$(R)
0.9	0.42	0.997	0.99	17.65		0.902	0.581	118.27		Phen.

Table 6 Optical parameters and quadrupole deformation parameter and length extracted from the analysis of ^{6}Li inelastic scattering to the first (2+, 4.44 MeV) excited state of ^{12}C at 600 MeV using the CC technique

Potential	Phen.	S1Y(R)	$t\rho\rho$(R)
δ_2^W (fm)	1.2	1.3	1.2

the experimental data. We have nonetheless checked in one of the analyzed data sets the effect of varying the range t upon the scattering cross-section.

3. The DF potential has been analytically derived using the $t\rho\rho$ approximation and the second-order (double-scattering) correction to the $t\rho_1\rho_2$ potential from Eqs. 9 and 12.
4. A new phenomenological formula was considered [26] to calculate the in-medium NN cross-section with $t\rho\rho$ calculations. In the present study we used ρ (the nuclear matter density)$=0.\,\mathrm{fm}^{-3}$ in Eq. 16.
5. The DF potentials generated from Eq. 5, using the S1Y and $t\rho\rho$ NN interactions, were fed into the computer code HI- OPTIM-94 [35]. The same potentials were fed into the computer code DWEIKO [37] to perform the same calculation with the approximate solution. Two options were considered: In the first, we compared the complex DF potentials predictions directly with the data; in the second option, we constructed the real DF potential in conjunction with an imaginary phenomenological WS volume shape.

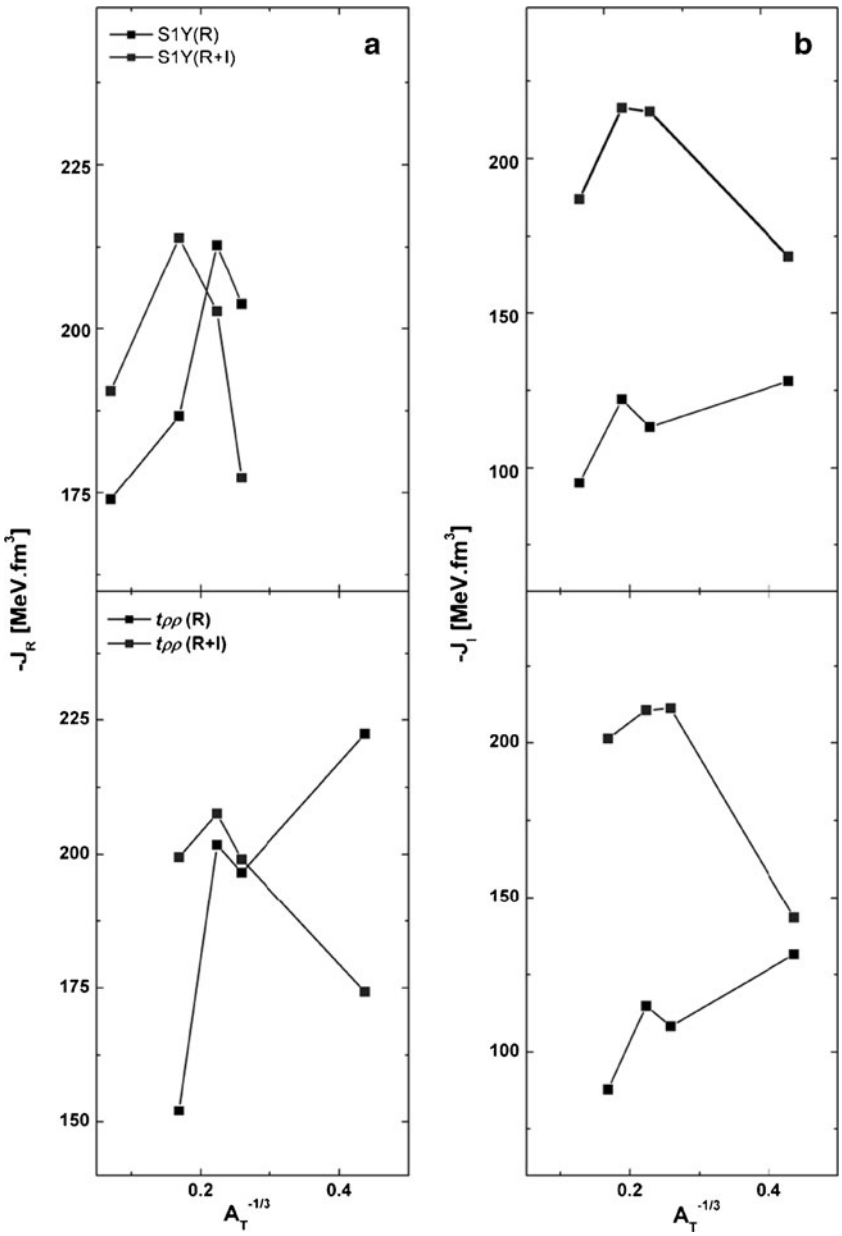

Fig. 7 Target mass-number dependence of the real and imaginary volume integrals obtained from the best-fit DF potentials

6. Routine searches were performed on two free parameters (the real and imaginary renormalization factor N_R and N_I) for the complex potential while four free parameters were searched in the other option [N_R besides the WS imaginary potential parameters (W_0, r_I, and a_I) were considered for the other potentials].
7. The deformation optical potentials were fed into the computer code CHUCK3 [38] to study the 2^+ low excited state, and the deformation parameter β and deformation length δ were calculated for both a single channel (DWBA) and CC.

4 Results and Discusion

We want to assess the ability of the constructed DF optical potentials, built upon the S1Y effective NN interaction and $t\rho\rho$ approximation, to describe ^{6}Li on ^{12}C, ^{58}Ni, ^{90}Zr, and ^{208}Pb elastic and inelastic scattering cross-sections at 100A MeV energy. Figures 1, 2, 3, 4, 5, 6, 11, 12, and 13 compare experimental elastic and inelastic scattering data with the theoretical predictions from the microscopically derived potentials.

4.1 Elastic Scattering

The derived DF potentials are employed to calculate the angular distribution of elastic scattering differential cross-sections for the ^{6}Li elastic scattering. The results are shown in Figs. 1, 2, 3, 4, 5, and 6, compared with the corresponding experimental data as well as with those produced by the phenomenological WS potentials. The optimal real and imaginary strengths (v and w) for the S1Y interaction, the renormalizing factors N_R and N_I for the $t\rho\rho$ interaction, and the phenomenological WS parameters are given in Tables 2, 3,

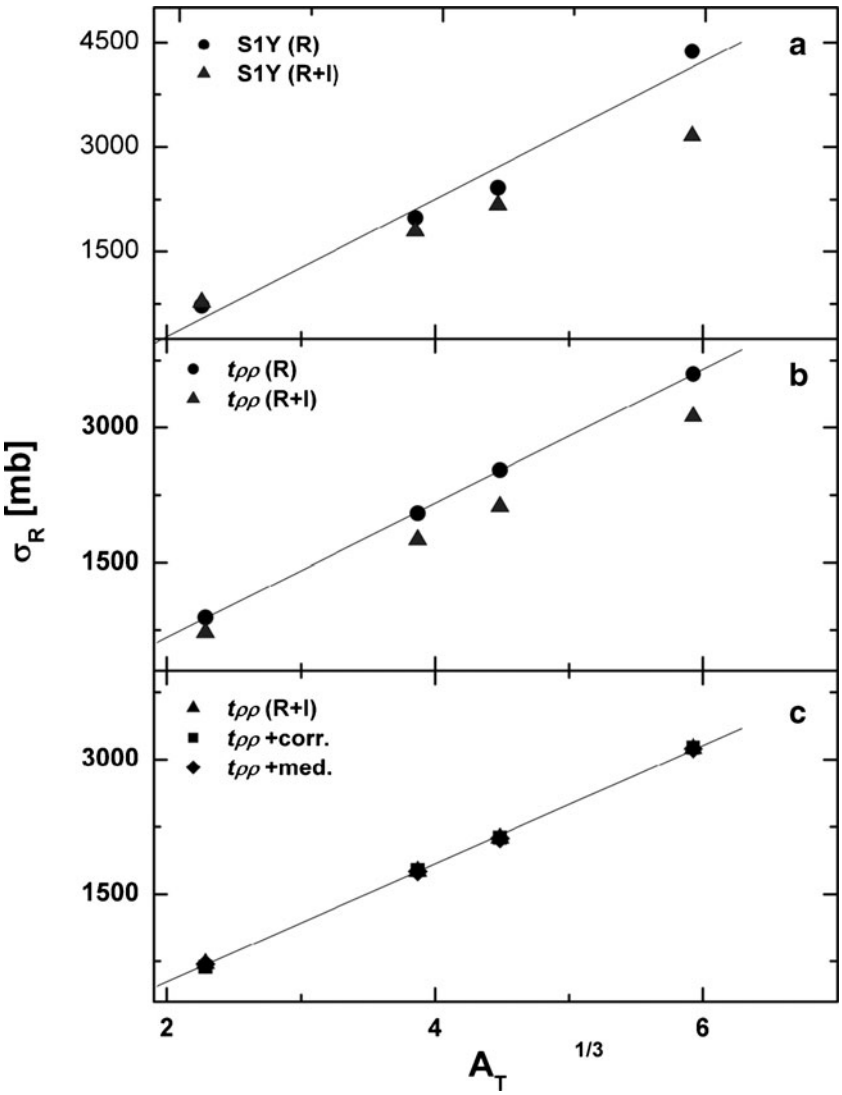

Fig. 8 Target mass-number dependence of the reaction cross-section σ_R extracted from the analysis of the ^{6}Li scattering

and 4, along with the associated volume integrals and predicted total reaction cross-sections.

First, in Figs. 1, 2, and 3, we present the results of the exact calculations. Figure 1 shows the cross-sections generated using the real DF potentials based upon the S1Y interaction (S1Y(R)) supplemented by phenomenological imaginary WS potentials and the corresponding complex DF ones (S1Y($R+1$)). The cross-sections are compared with phenomenological potentials results and corresponding experimental data. We see that the phenomenological potentials produce the best agreement with the data all over the measured angular range. The S1Y(R) potentials are more successful in describing the data than the S1Y(R+I) potentials. However, in general, both S1Y(R) and S1Y(R+I) potentials produce reasonable descriptions of the data. The results are comparable to those of Schwarz et al. [2], who used the DDM3Y potentials and CDCC method. The best-fit values of υ and w, shown in Tables 2 and 3, are larger than the values extracted by Satchler [19] at the corresponding energy (100A MeV).

The calculation based on the $t\rho\rho$ approximation for both real ($t\rho\rho(R)$) and complex potentials $t\rho\rho(R+I)$ are shown in Fig. 2. These potentials successfully reproduce the scattering data. The best-fit N_R and N_I are 0.6±0.06 and 0.75±0.15, respectively. These values are similar to those found by El-Azab and Hassanian [13] from the analysis of ^{6}Li over the energy range 76–380 MeV using DF potentials based upon the DDM3Y effective NN interaction. As already mentioned, we considered two modifications of the $t\rho\rho$(R+I) potential: the in-medium effect and the second-order (double-scattering) correction. Figure 3 shows the results. The second-order correction improves the qualitative features of the angular distributions, while the in-medium effect has negligible influence upon the curves. Tables 2 and 3 show that the depths of the folded potentials, represented by υ, w for the S1Y potential and N_R, N_I for the t$\rho\rho$ potentials have similar behaviors. Except for the ^{12}C target, insertion of the second-order correction reduces N_R and increases N_I. For the ^{12}C target, the in-medium effect reduces both renormalization factors.

Second, we present the DWEIKO-code [37] calculations based on the eikonal approximation using the previously derived potentials. We generate the elastic scattering differential cross-sections of the considered

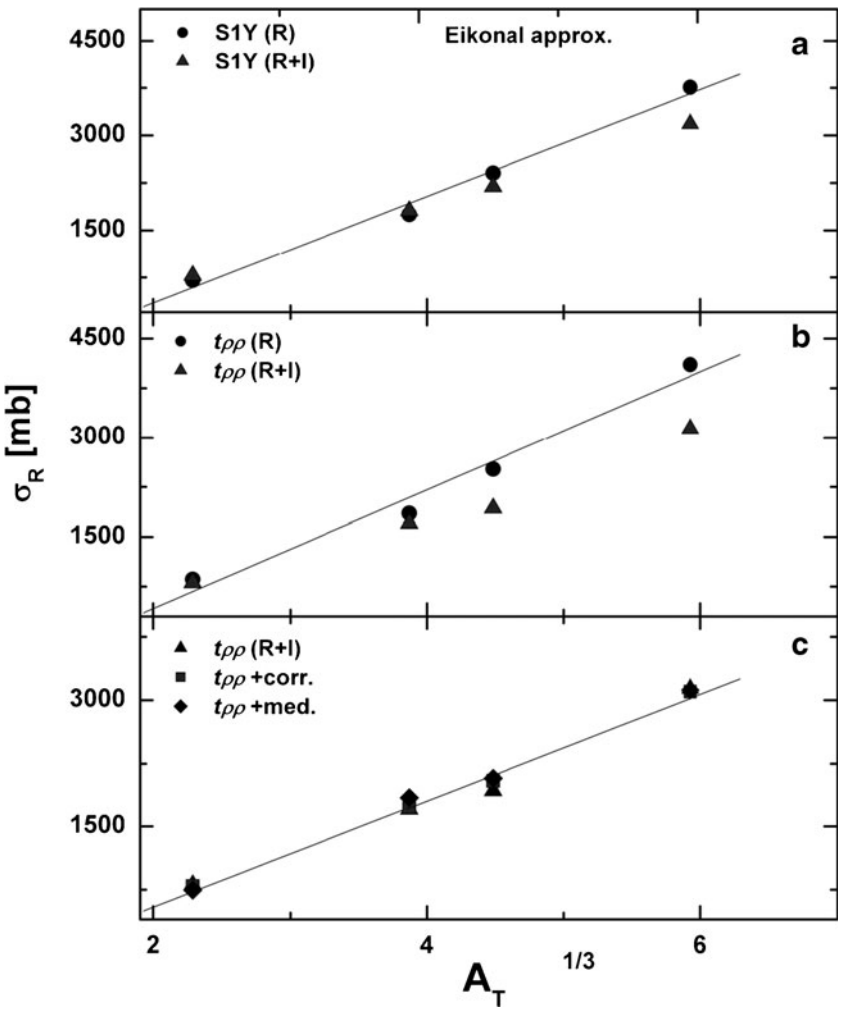

Fig. 9 Target mass-number dependence of the reaction cross-section, as in Fig. 8, but for the eikonal approximation

reactions and list the corresponding best-fit parameters in Tables 4, 5, and 6. The extracted cross-sections are plotted in Figs. 4, 5, and 6. Almost no change is found in the parameters of the real and imaginary folded potentials. Figure 4 shows that the S1Y(R) potential best describes of the data. The phenomenological potential substantially overestimates the ^{12}C target data throughout the angular range $\theta_{\mathrm{c.m}} \approx 15$–25. This result is similar to that of Schwarz et al. [2] for the same target. Reasonable fits of the data are obtained for the other targets. Figure 5 shows that also the $t\rho\rho$ potentials overestimate the data at the backward angles for the ^{12}C target. In general, reasonable fits to the data are obtained for the other targets.

Evident in Fig. 4 is a discrepancy between the $t\rho\rho$ real DF potentials and those corrected by the medium effect and high order correction, especially at small radius. By contrast, these potentials agree quite well at $R \geq R_{\mathrm{SA}}$. The corresponding imaginary DF potentials have the same behavior. In comparison with the $V^{(2)}_{A_1A_2}(R)$ potential, the range of the second-order potential is appreciably shorter than that of the first one, owing to the high order density dependence $((t\rho_1)\rho_2)^2$ versus $((t\rho_1)\rho_2)$ [24]. Therefore, the form of $\mathrm{Re}V^{(2)}$ in Eq. 13, which is linear in $\mathrm{Ref}_{\mathrm{NN}}$ (corresponding to the parameter α), is attractive at energy 100A MeV. As shown by Fig. 4, the real part of the potential $\left(V^{(2)}_{A_1A_2}(R) + V^{(1)}_{A_1A_2}(R)\right)$ is much deeper than $V^{(1)}_{A_1A_2}(R)$. The relative difference between $V^{(2)}_{A_1A_2}(R) + V^{(1)}_{A_1A_2}(R)$ and $V^{(1)}_{A_1A_2}(R)$ is 22±1% for the considered reactions. By contrast, Im $V^{(2)}$ behaves as $\alpha^2 - 1$, $\alpha > 1$, so that the imaginary part for potential $\left(V^{(2)}_{A_1A_2}(R) + V^{(1)}_{A_1A_2}(R)\right)$, as shown in Fig. 5, is shallower than the potential $V^{(1)}_{A_1A_2}(R)$, and the ratio between $V^{(2)}_{A_1A_2}(R) + V^{(1)}_{A_1A_2}(R)$ and $V^{(1)}_{A_1A_2}(R)$ equals 5.5±0.5% for these reactions. Figure 6 shows how the second-order correction and in-medium effect in the calculated potentials affect the obtained angular distributions of the differential cross-section. Clearly, the second-order correction both qualitatively and quantitatively improves

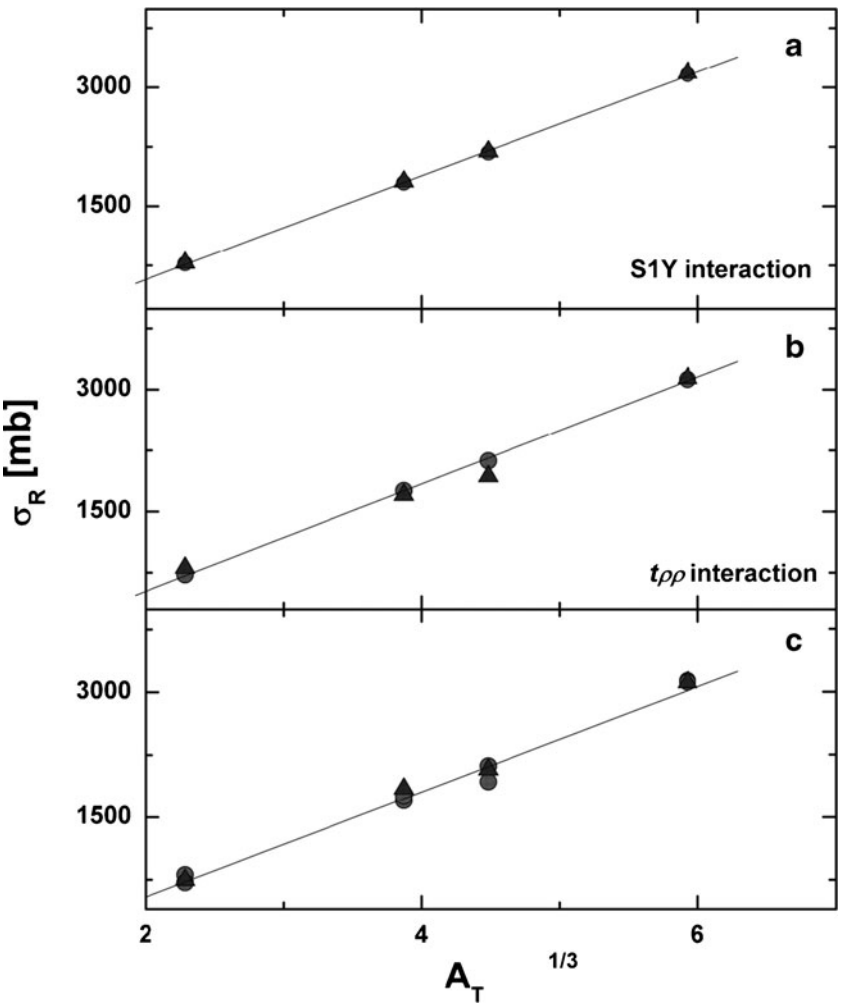

Fig. 10 Comparison between the reaction cross-sections σ_R extracted from the exact and eikonal treatments

the description of the data. On the other side, the in-medium treatment slightly improves the fits to data, except for the ^{58}Ni target.

4.2 Inelastic Scattering

The theoretical predictions of the angular distribution of the differential inelastic scattering cross-sections are shown in Fig. 11, compared with the experimental data. The upper panel shows the results of the DWBA and the bottom panel, those of the CC technique. Clearly, the S1Y(R) potential best fits the data, in both the DWBA and CC treatments. The S1Y(R) and $t\rho\rho$ (R) potentials yield almost identical predictions with the CC mechanism. In the DWBA calculation, the phenomenological and $t\rho\rho$ (R) potentials underestimate the data at $\theta_{c.m}>15°$. Figure 12 shows the results for the real and complex S1Y potentials using the CC calculations and the feedback to elastic scattering channel in comparison with the experimental data. As shown from both figures, the experimental data are successfully reproduced. Similar comparisons for the $t\rho\rho$ potentials are shown in Fig. 13. Comparison between Figs. 11 and 13 highlights the importance of the CC mechanism.

4.3 Volume Integrals

For further discussion, the potentials can be classified by their real and imaginary volume integrals per interacting nucleon pair. The volume integral is a sensitive measure of the potential strength. The obtained volume integrals of the best-fit real folded potentials (J_R) and of the associated imaginary potentials (J_W) for the ^{6}Li elastic scattering from the considered target nuclei are listed in Tables 2 and 3, respectively. Many studies, e.g., El-Azab Farid and Hassanain [13] [14], have investigated the target mass number dependence of J_R and found that J_R decreases as the target mass number

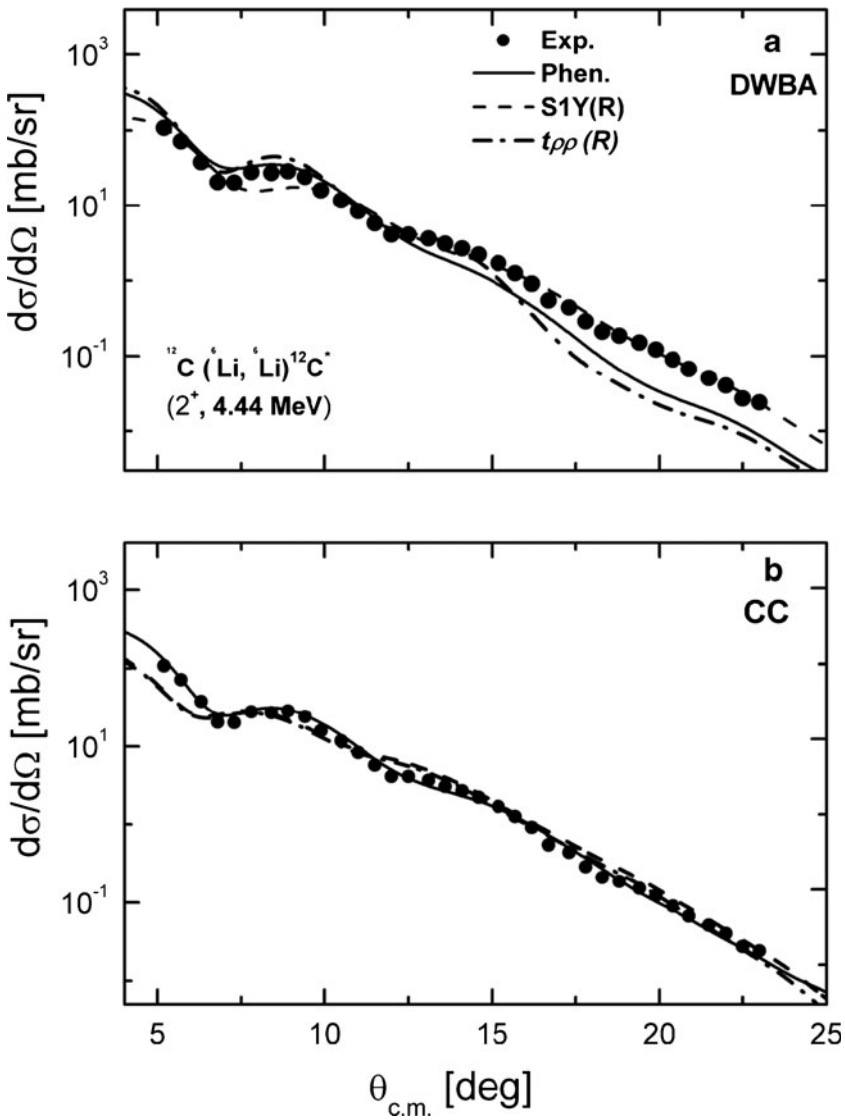

Fig. 11 Angular distributions of the inelastic scattering cross-section (2+, 4.44 MeV) for ^{6}Li+^{12}C at 600 MeV using the phenomenological and extracted potentials via the DWBA and CC techniques

grows. This was attributed to the increased Pauli blocking effects [39, 40]. From the analysis of ^{6}Li elastic scattering on the light targets at low energies, Gupta and Murthy [41] proposed the following linear−in−$A_T^{-1/3}$ relation for this dependence:

$$J_R = -C\left(1 + DA_T^{-1/3}\right)\text{MeV.fm}^3, \tag{21}$$

where C=147 MeV fm^3 and D=2.0. Nadasen et al. [39, 40] obtained a similar $A_T^{-1/3}$−linear relation from the 210 MeV data using the phenomenological optical-model potentials, with different coefficients, C=215 MeV fm^3 and D=0.88. In this work, we have compared the J_R and J_I resulting from the generated DF potentials using $t\rho\rho$ and S1Y interactions with $A^{-1/3}$ at 100A MeV. This mass dependence is shown in Fig. 7. The left and right panels display the real volume integral J_R and the imaginary volume integral $J_{I,}$ respectively. In each plot, we only have four points, a number too small to realistically determine the behavior of the results.

4.4 Total Reaction Cross-Sections

With the above-described formalism, using the derived potentials in the framework of the exact solution and eikonal approximation, we have computed the total reaction cross-section σ_R for ^{6}Li ions colliding with ^{12}C, ^{58}Ni, ^{90}Zr, and ^{208}Pb targets at 100A MeV. The results are listed in Tables 2, 3, and 4. Figure 8 shows the target mass-number dependence of σ_R, which is clearly linear for all potentials. In general, the σ_R from the complex folded potentials are slightly lower than those found from real folded potentials supplemented by phenomenological imaginary WS potentials. Also, it is clear from the lower part of Fig. 8 that σ_R is insensitive to the second-order and in-medium corrections. The slopes of the three plots in Fig. 10 are equal and consistent with the slope

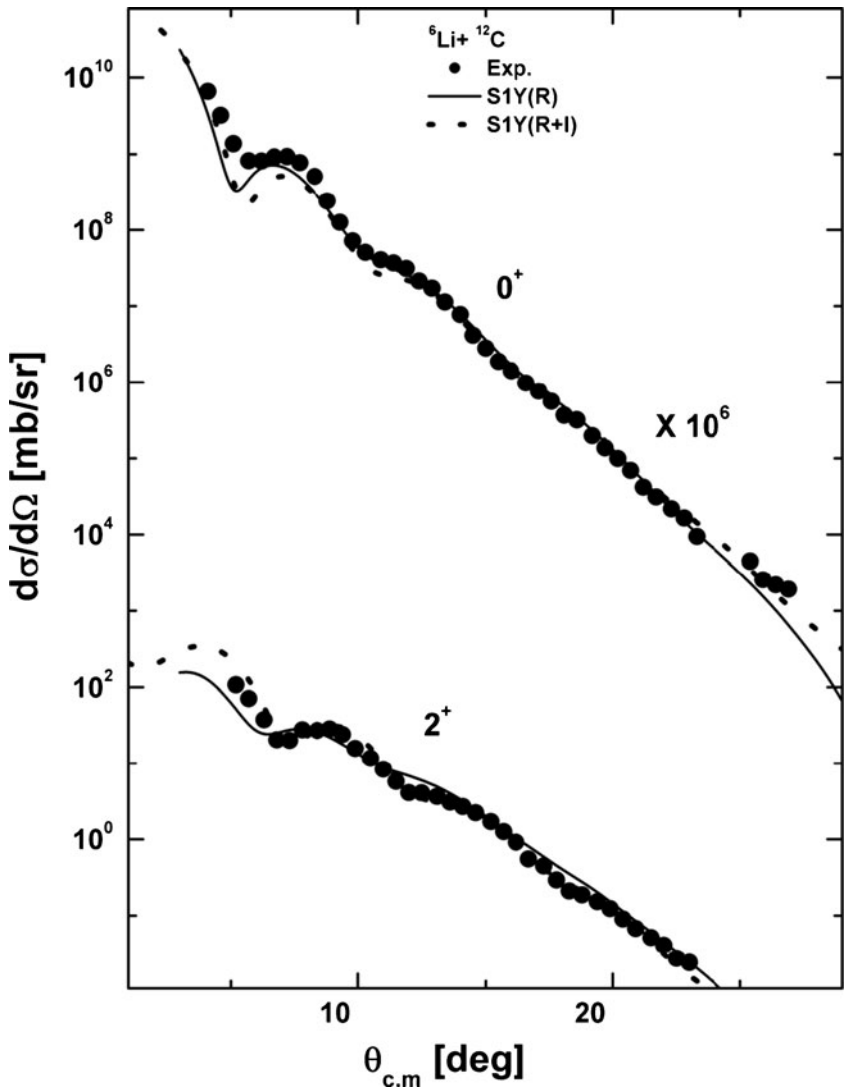

Fig. 12 Elastic and inelastic scattering cross-sections for ^{6}Li+^{12}C at 600 MeV using the S1Y (R) and S1Y (R+I) potentials

previously found at lower energies [12, 13]. Similar conclusions can be extracted from Fig. 9 for the eikonal approximation calculations. Figure 10 compares σ_R computed from the exact expression with eikonal-approximation calculations. It is evident that both methods yield identical results. This indicates that the eikonal approximation is reliable to calculate the σ_R at the considered bombarding energy, a result similar to that obtained by Rajendra et al. [42] at the same energy. Figures 8, 9, and 10 show that σ_R has strongly linear dependence on the cubic root of the target mass number, a result consistent with that found in the previous studies [13, 14, 42].

At low energies, the calculation will most likely be improved by corrections to the impulse approximation ($t-$matrix amplitude) correlation effects [43], or perhaps relativistic effects [44]. It is evident from the calculated σ_R of ^{6}Li scattering in Tables 2 and 3 that the σ_R calculated from the ($V^{(2)}(R)+V^{(1)}(R)$) potentials are 2 % smaller than those calculated with $V^{(1)}(R)$. At this energy, the percentage difference between the exact calculation and eikonal approximation solutions are slightly smaller, as shown by Fig. 10, a result that gives confidence on the eikonal approximation at the considered energy (Figs. 11, 12, and 13).

5 Conclusions

We have analyzed the recently measured data on ^{6}Li scattering from ^{12}C, ^{58}Ni, ^{90}Zr, and ^{208}Pb at 100A MeV. Our calculations have been divided into two main parts. The first analyzed the data on ^{6}Li elastic and inelastic scattering at 100A MeV using the constructed complex DF optical potentials, where both real and imaginary parts are renormalized by two different factors. In the other option, the real DF potential is combined with a phenomenological imaginary one in a WS form. The derived potentials from both options yielded reasonable fits to

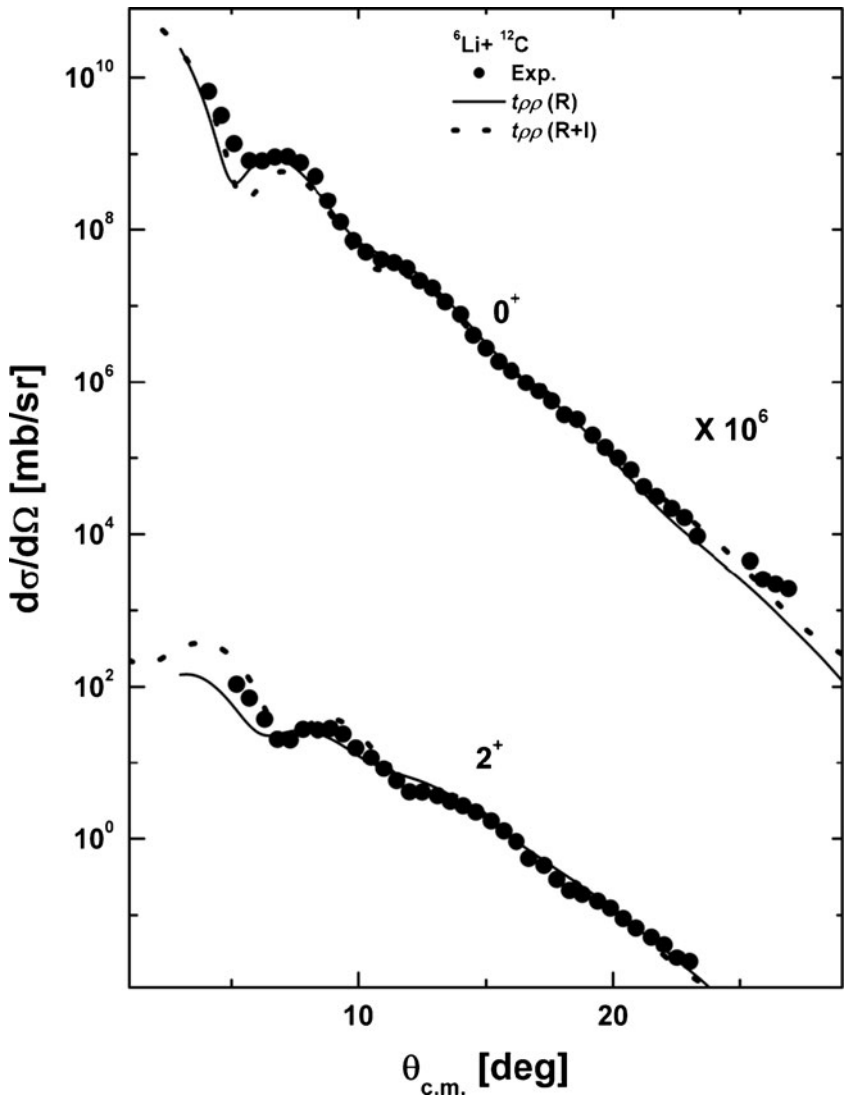

Fig. 13 Elastic and inelastic scattering cross-sections, as in Fig. 12, but for the $t\rho\rho$(R) and $t\rho\rho$(R+I) potentials

the experimental data. However, in general, the success of the latter potential to describe the data is more pronounced than that of the former. This may be attributed to the added flexibility provided by the four free parameters in the optimization.

The obtained best-fit values for the real and imaginary S1Y interaction are larger than those expected by Satchler at the corresponding energy (100A MeV). Improved agreement with experimental data has been obtained using the exact solution with the first option (complex DF potential) when Pauli blocking was used or when the higher-order term of multiple scattering was added. The medium effect works well in the eikonal approximation and improves the agreement with experiments. We conclude that the second-order (double scattering) potential and in-medium correction have more impact on the eikonal-approximation calculations than on exact-solution calculations.

To validate the generated DF potentials, we have employed the transition folded potentials derived from the transition density of ^{12}C to analyze the only available reaction data on ^{6}Li inelastic scattering to the first (2^{+}, 2.44 MeV) excited state 100A MeV. Two methods were employed, the DWBA and CC techniques. The performance of the DWBA was shown to be more successful than the CC technique, due to the weak coupling between elastic and non-elastic channels at high energies.

References

1. Rituparna Kanungo, T. Sinha, C. Samanta, Subinit Roy, A. Chatterjee, B.J. Roy, S. Ray, Nucl. Phys. **A599**, 579 (1996)
2. K. Schwarz et al., Eur. Phys. J. **A7**, 367 (2000)
3. K. Ruesk, N. Almamanos, N. Keeley, V. Lapoux, A. Pakou, Phys. Rev C **70**, 014603 (2004)
4. G. Baur, H. Rebel, Ann. Rev. Nucl. Part. Sc. **48**, 321 (1996)
5. Y. Sakuragi, M. Yhiro, M. Kamimora, Prog. Theor. Phys. Suppl. **89**, 136 (1986)
6. Y. Sakuragi, M. Ito, Y. Hirabayashi, C. Samanta, Prog. Theo. Phys. Lett. **98**, 521 (1997)
7. R. Kanungo, M. Lahiri, C. Samanta, H. Rebel, Int. J. Mod. Phys. E **4**, 827 (1995)
8. G.R. Satchler, W.G. Love, Phys. Rep. **55**, 183 (1979)
9. R.M. Devries et al., Phys. Lett. **39**, 450 (1977)
10. H. Amakawa, K.I. Kubo, Nucl. Phys. **A266**, 521 (1976)
11. Y. Sakuragi, Phys. Lett. **B220**, 22 (1989)
12. M. El-Azab Farid, G.R. Satchler, Nucl. Phys. **A438**, 525 (1985)
13. M. El-Azab Farid, M.A. Hassanain, Nucl. Phys. **A678**, 39 (2000)
14. M. El-Azab Farid, M.A. Hassanain, Nucl. Phys. **A697**, 183 (2002)
15. M. El-Azab Farid, M.A. Hassanain, Eur. Phys. J. **A19**, 231 (2004)
16. C. Samanta, Y. Sakuragi, M. Ito, M. Fujiwara, J. Phys. G: Nucl. Part. Phys. **23**, 1697 (1997)
17. G. Bertsch, J. Borysowicz, H. Me Manus, W.G. Love, Nucl. Phys. **A284**, 399 (1977)
18. Z. Majka, H.J. Gils, H. Rebel, Z. Phys. **A288**, 139 (1978)
19. G.R. Satchler, Nucl. Phys. A **579**, 241 (1994)
20. O.M. Knyazov, E.F. Hefter, Z. Phys. A **301**, 277 (1981)
21. J.P. Jeukenne, A. Lejeunne, C. Mahaux, Phys. Rev. C **16**, 80 (1977)
22. G.R. Satchler, *Direct Nuclear Reactions* (Clarendon, Oxford, 1983)
23. H. Feshbach, A. Gal, J. Hufner, Ann. Phys. **66**, 20 (1971)
24. M.S. Hussein, R.A. Rego, C.A. Bertulani, Phys. Rep. **201**, 279 (1991)
25. L. Ray, Phys. Rev. C **20**, 1857 (1979)
26. R.J. Glauber, *In lectures on theoretical physics* (Interscience, New York, 1959)
27. W.J. Wilson, W. John, Phys. Lett. **B52**, 149 (1974)
28. S. Kox et al., Phys. Lett. **B159**, 15 (1985)
29. K.H. Bray, M. Jain, K.S. Jayaraman, G. Lobianco, G.A. Moss, W.T.H. Oers, D.O. Wells, F. Petrovich, Nucl. Phys. **A189**, 35 (1972)
30. M. Jaminon, C. Mahaux, Phys. Rev. C **34**, 2097 (1986)
31. S.K. Gupta, Z. Phys. **A331**, 457 (1988)
32. E. Boridy, H. Feshbach, Ann. Phys. (NY) **109**, 468 (1977)
33. C. Xiangzhou et al., Phys. Rev. C **58**, 572 (1998)
34. H.V. Von Geramb, *Microscopic optical potentials* (Springer, Berlin, 1979)
35. N. M. Clarke, Computer Program, (1994) (unpublished)
36. A. Nadasen et al., Phys. Rev. C **47**, 674 (1993)
37. C.A. Bertulani, C.M. Campell, T. Glasmacher, Comput. Phys. Commun. **152**, 317 (2003)
38. P. D. Kunz, Computer Program, (1984) (unpublished)
39. A. Nadasen et al., Phys. Rev C **37**, 132 (1988)
40. A. Nadasen et al., Phys. Rev C **39**, 536 (1989)
41. S.K. Gupta, K.H.N. Murthy, Z. Phys. A **307**, 187 (1982)
42. R.D. Rajendra, S.K. Govind, A.C. Francis, M.M. Khin, NASA, TP-3498 (1995)
43. P.E. Hodgson, Adv. In Phys. **15**, 329 (1966)
44. R.R. Roy, B.P. Nigam, Nuclear physics, *Theory and Experimental,* (New York, 1967)